# Chapter 7

# Instrumentation and Techniques in High Energy Physics: Liquid Argon Neutrino Detectors

David Caratelli

*Department of Physics, Broida Hall*
*University of California, Santa Barbara, CA 93106-9530*
*dcaratelli@ubcs.edu*

Liquid Argon Time Projection Chambers (LArTPCs) have become a prominent detector technology employed in experimental neutrino physics. This chapter presents a review of the LArTPC technology, with an emphasis on its use in large-scale neutrino experiments which study MeV to GeV neutrino interactions from accelerator or astrophysical sources. First, we provide a description of how these detectors came about and what motivates their construction in Section 7.1. Next, we describe the operational principle of LArTPC detectors, covering how signals are formed (Section 7.2), propagated (Section 7.3), and detected (Section 7.4). We then conclude with a description of how signals from LArTPCs are reconstructed and analyzed, and provide a brief overview of how such detectors are calibrated in Section 7.5.

## 7.1 Introduction: Why and How LArTPC Neutrino Detectors Came About

In the literature, several people are often highlighted for their contributions to the development of the LArTPC technology. The potential for liquid argon detectors as fully active detectors for particle physics was recognized by Willis and Radeika [1] and Nygren [2] in the early 1970s. Their

 https://doi.org/10.1142/9789819801107_0007

applicability to neutrino detection was put forward by Rubbia [3] and others [4] shortly after. Since these early proposals, the successful development of the technology came about thanks to the effort of entire communities tied to research in detector instrumentation, electronics, engineering, software, and offline tool development. Before delving into a description of the technology itself, it is worth understanding why and how this detector technology came to be such a significant player in experimental neutrino physics.

Detectors are developed because they solve a given technological challenge. Liquid argon neutrino detectors do so in two fundamental ways: they provide fully instrumented large-mass targets for neutrino interactions and do so while faithfully tracking with millimeter accuracy the particles produced in such interactions. These features address the need for large-scale detectors in neutrino experiments, where event statistics are a precious commodity, and satisfy an important requirement to accurately measure the leptons and hadronic system needed to reconstruct the neutrino flavor and energy which are input to neutrino oscillation measurements. LArTPCs achieve this by leveraging argon's large yield of ionization charge and scintillation light. In this way, the detector acts both as the active target for incoming neutrinos and the source of ionization charge and scintillation light signals. Transport of the charge signals through a uniform electric field allows us to efficiently instrument a single 2D detector wall while preserving the 3D pattern of charge deposition, providing accurate 3D imaging capabilities. Finally, the ability to instrument such a detector with modern readout electronics elevates the bubble chamber like imaging capabilities of a LArTPC providing detailed calorimetric information necessary for quantitative measurements with modern computing tools. These features combined make the LArTPC an ideal technology for precision measurements of neutrino interactions and oscillations. The exquisite imaging capabilities of the LArTPC further enable searches for rare interaction modes which are the signature of Beyond the Standard Model (BSM) physics. These searches often complement the experimental program at intense neutrino beam facilities.

Making the simple detection principle of the LArTPC a reality has required significant technological development. Advances in cryogenic engineering as well as argon purification have made possible constructing large-scale detectors which allow for the efficient propagation of electron and photon signatures over meter-scale distances. Low-power electronics that operate in liquid argon with high channel count have enabled high-resolution imaging with low noise. Advances in computing and analysis

methods have made the study of dataset comprising $\mathcal{O}(10^6)$ neutrino interactions a reality. These are only some of the developments that have contributed to making the LArTPC technology successful today. While this chapter provides a comprehensive overview of the operation and performance of liquid argon neutrino detectors, further references can provide more detailed information. Of note are references that discuss aspects of instrumentation and detector performance tied to this technology. Reference [5] detailing the performance of the 3-ton prototype for the ICARUS experiment, a launching pad for the development of this detector technology, provides a comprehensive overview of many detector effects and operation parameters. The "Detector Papers" from ICARUS [6, 7], MicroBooNE [8], LArIAT [9], and protoDUNE [10, 11] are useful references that discuss in detail the design of important LArTPC detectors while also providing insight into detector design, construction, and operation more broadly. More references from the broad literature of liquid argon neutrino experiments tied to specific subsystems, detector effects, or calibration methods are provided throughout this chapter when relevant.

### 7.1.1 *Operational principle of a LArTPC*

This section gives a practical overview of how a LArTPC is used to image neutrino interactions. The many concepts and detector components introduced here are expanded on in subsequent sections. A neutrino LArTPC aims to detect the visible signature of neutrino interactions comprised of the ionization charge and scintillation light produced as charged particles propagate through the detector. Figure 7.1 shows a schematic of the main components of a TPC and how ionization electrons are used to record signals on the electronics. A uniform electric field is applied across the TPC through a negative potential on the cathode plane. This field causes ionization electrons to drift toward the anode, where charge sensors (wires or pixels) record the current induced by the drifting electrons, or collect their charge directly. Each sensor records an analog pulse associated with the drifting electron cloud. The uniform drift allows ionization electrons recorded at the anode to faithfully map out the 3D pattern of energy deposition produced by charged particles resulting from the neutrino interaction. Multiple wire planes, oriented at different angles, are used to record multiple complementary signatures of the same ionization electron cloud. Time-coincident signals on different wire planes can then be used to "triangulate" the charge and obtain the exact 2D coordinate for the ionization cloud on the 2D wire plane. Finally, the depth in the detector

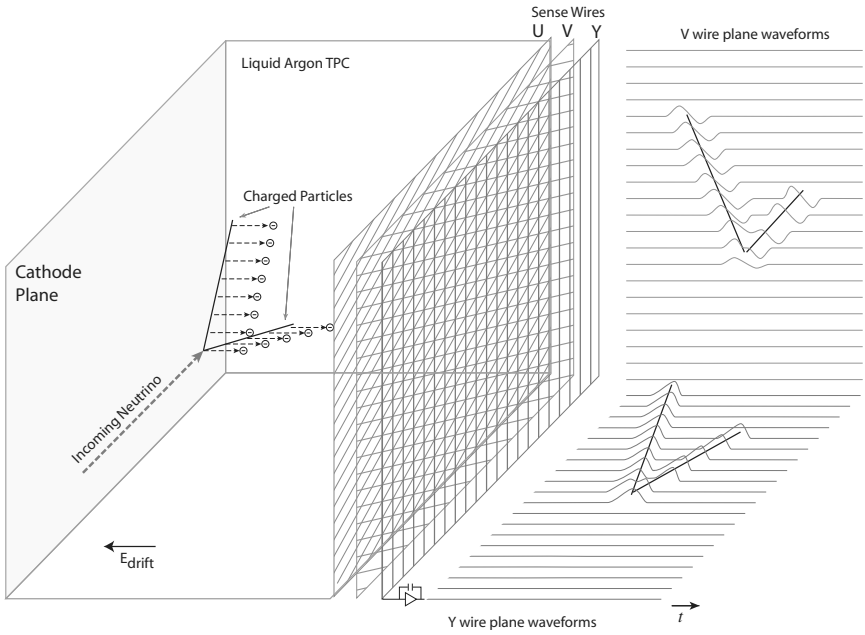


Figure 7.1. Cartoon depicting the operational principle of a LArTPC. Ionization charge drifts uniformly across the detector volume, producing signatures on different sense wire planes which when combined in offline reconstruction are used to recover the 3D charge deposition pattern.

*Source*: Figure from Ref. [8].

along the direction of the electric field can be calculated leveraging the fact that electrons drift at a constant speed of $\mathcal{O}(1)$ mm/$\mu$s. The TPC provides full 3D information up to a degeneracy in the absolute distance of energy deposition along the direction of the electric field associated with the drift velocity. Breaking this ambiguity requires an independent measurement of the interaction time which is provided by the scintillation light. Scintillation photons travel across the detector in a few ns but unlike ionization electrons propagate isotropically. Collecting them while maintaining the uniform and fully active nature of the TPC requires placing light sensors — typically Photo Multiplier Tubes (PMTs) or Silicon Photo-Multipliers (SiPMs) — on the edge of the TPC, often right behind the anode plane. Scintillation light provides accurate timing which is essential for absolute 3D position reconstruction as well as background rejection in surface-based LArTPC detectors studying GeV–scale neutrino interactions.

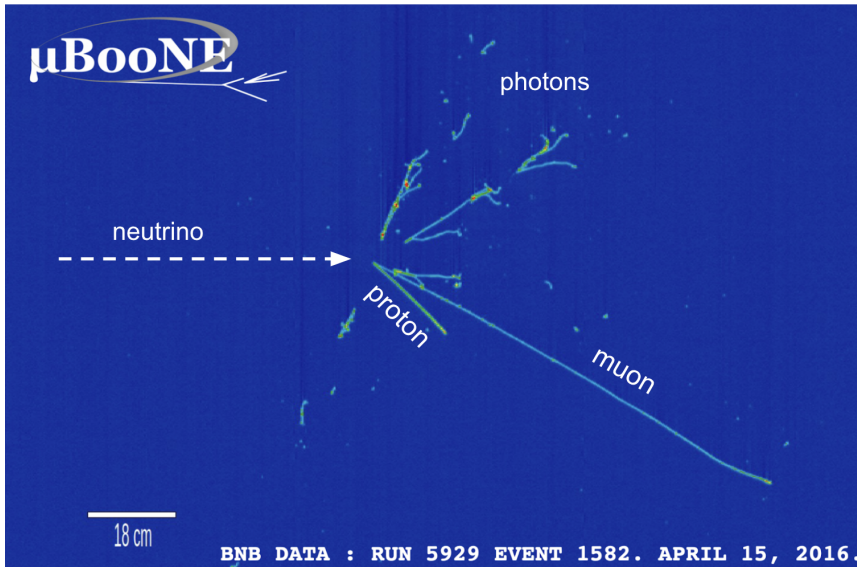


Figure 7.2. Event display showing a candidate neutrino interaction recorded with the MicroBooNE LArTPC. The 2D image shows the signals recorded on the wires of one of the three wire planes with which the detector is instrumented. Data from each wire is represented as a vertical strip in the image, with the vertical axis denoting the recorded time of the signal on the wire. The color scale in the image denotes the amount of charge collected. The large portions of blue in the image represent regions with no collected signals. The neutrino (which originates from the beam and enters from the left in the image) is not directly visible in the detector but produces charged particles which ionize the argon and leave behind trails of ionization electrons. The activity in green and red is the signature of these ionization electrons as recorded on the sense wires. The topology and charge profile of the ionization pattern can be leveraged to reconstruct each particle's species and its kinematics.

*Source*: Figure reproduced from microboone-exp.fnal.gov.

In addition to providing millimeter-scale position resolution on final-state particle trajectories, the large signal-to-noise of modern LArTPC detectors provides up to percent-level charge resolution for individual energy deposits on the collection wires and thresholds of $\mathcal{O}(100$ keV). Figure 7.2 shows a neutrino interaction candidate collected with the MicroBooNE LArTPC with several final-state particles coming out of the interaction vertex. The charge collected on the wires, represented by the color scale on the figure, measures the energy loss profile which is used for calorimetric energy measurements as well as particle identification (PID).

### 7.1.2 *Experimental landscape in the early 2020s*

Liquid argon neutrino detectors are now at the forefront of the experimental neutrino physics program aiming to perform precision measurements of neutrino oscillations and search for new physics. This experimental program, international in nature, is centered around Fermilab's intense neutrino beams which provide a focused source of 0.1–10 GeV neutrinos delivering $1\text{–}10 \times 10^{20}$ protons on target (POT) per year. Two experimental projects currently make use of the LArTPC technology in Fermilab's neutrino beamline: the Short Baseline Neutrino (SBN) program [12] and the Deep Underground Neutrino Experiment (DUNE). Available references in the literature provide a useful overview of the SBN [13] and DUNE [14–16] experimental programs. Here, we provide a brief summary of both to help better contextualize the LAr neutrino detector description in relation to the physics being pursued.

The physics reach of this program is very broad and encompasses several areas. Driving the detector and beam design is the precision measurement of neutrino oscillations, with emphasis on the measurement of the $\delta_{CP}$ violating phase in the lepton sector, and the neutrino mass ordering with DUNE. The broader DUNE and SBN programs have a varied BSM physics program which leverages the intense neutrino beams as a possible source of new particles produced through feeble couplings to the standard model. The DUNE far detectors, thanks to their underground location, serve as a unique astrophysics observatory for neutrinos from a possible galactic supernova burst and from solar neutrinos. The quiet far detector environment further makes the experiment well suited for searches for proton decay or neutron-antineutron oscillation which test fundamental symmetries. Finally, the SBN program provides a venue for key measurements of neutrino scattering on argon, an important source of systematic uncertainty for oscillation measurements and BSM searches alike. The breadth of this program is possible in part thanks to the versatile capabilities of the LArTPC detector's ability to image interactions with exceptional resolution across the MeV to several GeV energy regime.

The SBN program is comprised of three LArTPC detectors placed at different distances from the neutrino beam target. The three detectors are the Short Baseline Neutrino Detector (SBND), the MicroBooNE detector, and ICARUS. In addition to multi-detector searches for eV-scale sterile neutrinos, each detector carries out an independent physics program. The MicroBooNE experiment [8] collected data from 2015 to 2021, making it

the longest-running LArTPC experiment to date. Throughout this time, MicroBooNE has played a key role in transforming the LArTPC technology into one capable of delivering high-precision measurements of neutrino interactions with advanced analysis techniques with large-scale datasets. This includes MicroBooNE's first results investigating the nature of the MiniBooNE excess [17–21]. The ICARUS experiment [22] serves as the primary far-detector for the SBN program thanks to its 600 tons of active argon mass. The detector began data-taking in 2020. SBND, the near detector for the program, sits only ∼100 m from the beam target and is therefore exposed to a very large flux of neutrino interactions. This makes the SBND detector uniquely positioned for high-statistics measurements of neutrino–argon interactions and searches for rare processes tied to BSM signatures. The SBND detector is expected to begin data-taking in 2023.

DUNE will represent the culmination of the long-baseline oscillation program and leverages a powerful beam, longer baseline from the neutrino source, and large LArTPC active mass to achieve the statistics and precision needed for its oscillation physics program. The experiment is comprised of near and far detectors located in the Homestake mine in South Dakota and on the Fermilab campus, respectively. The detector is expected to start data-taking in the late 2020s, with a staging of the several modules and detectors which make up the experimental facility. The far detector, situated one mile underground at the Sanford Underground Research Facility in Lead, South Dakota, will additionally serve as a unique facility for the observation of astrophysical neutrinos from a galactic supernova burst and the Sun [15]. The near detector provides a rich physics program itself, centered on searches for BSM physics [16].

The development of the LArTPC technology benefits from a continuous stream of small-scale demonstrators and R&D test stands. Those that have documented their operations in the literature provide an invaluable source for readers interested in learning the details of hardware components, engineering requirements, cryogenic, DAQ, and many other topics related to the design, construction, and operation of a LArTPC. Details can be found in references from the LArPD [23] and LongBo [24] test stands at Fermilab, the ICARUS 3-ton demonstrator [5], and BNL's 20-liter test stand [25]. Large-scale prototype detectors such as the protoDUNE single [10, 11] and double-phase TPC complement this list and are providing insight for the construction of multi-kiloton LArTPC detectors in DUNE.

## 7.2 Particle Propagation and Signal Formation in Liquid Argon Neutrino Detectors

Liquid argon neutrino detectors take advantage of their ability to precisely track the path of charged particles propagating through the detector volume. This section describes how particles propagate in liquid argon and how signals of ionization charge and scintillation light are formed.

### 7.2.1 *What does a neutrino LArTPC see?*

Neutrino experiments rely on the detection of final-state particles produced in neutrino interactions. Of particular relevance to the study of neutrino oscillations is the signature of the charged lepton resulting from charged current neutrino interactions. This primarily means electrons and muons from $\nu_e$ and $\nu_\mu$ charged current (CC) interactions, respectively. The hadronic response in neutrino interactions from the MeV to the few-GeV scale is vastly complex and tied to the details of the neutrino interaction mode and effects that impact the propagation of particles through the argon nucleus. A review of such processes is outside of the scope of this text. Here we focus on describing how the most common particles produced in neutrino interactions propagate through and manifest themselves in LArTPC detectors. One of the features that make LArTPC detectors so powerful in the study of neutrinos is their ability to record with low threshold particles produced in the interaction's hadronic recoil. Photons, charged and neutral pions, protons, and neutrons are the most commonly produced particles for interactions of up to several GeV of energy. The description of particle propagation is subdivided between particles that are often referred to as "shower-like", such as electrons and photons, and those that are "track-like", such as muons, protons, and charged pions. A final section on the propagation of neutrons concludes this presentation. While the description presented centers on propagation in LAr, relevant background can be found in the PDG's "Passage of Particles through Matter" chapter of the Particle Data Group's "Review of Particle Physics" [26].

#### 7.2.1.1 *Propagation of electrons and photons*

The propagation of electrons and photons in argon is governed by Compton scattering and pair production for photons and ionization and Bremsstrahlung for electrons. Figure 7.3 shows the energy loss profile for

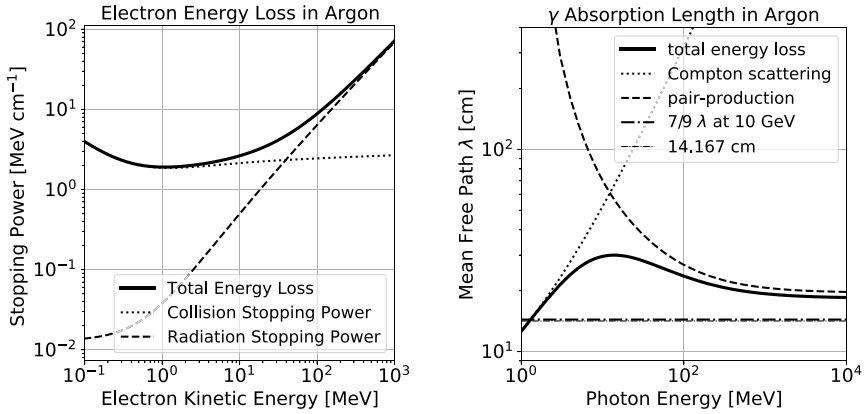


Figure 7.3. Left: Energy loss for electrons as a function of energy divided in the two primary components: Collision stopping power (or ionization) and radiative losses (Bremsstrahlung photon production). Right: Mean-free path for photons propagating in argon contributed by two main processes: Compton scattering and pair-production, dominating below and above 10 MeV, respectively.

electrons (left) and the interaction length for photons (right) as a function of energy. Pair production ($\gamma \rightarrow e^+e^-$) for photons and Bremsstrahlung ($e + N \rightarrow e + \gamma$) for electrons cause the propagation of these two particles to be interconnected and leads to the formation of electromagnetic (EM) cascades which manifest as "showers" in the detector. Energy has a significant impact on the topology of EM showers. Electrons and photons of several hundred MeV or more lead to fully developed EM showers that are easily recognized as such in the detector. As one approaches the $\mathcal{O}(100)$ MeV regime, the stochastic nature of pair production and Bremsstrahlung photon production lead to "fragmented" EM showers. Below $\mathcal{O}(100)$ MeV, EM showers appear largely as a single track-like ionization segment caused by an electron, followed by several isolated Compton scatters contributed by low-energy Bremsstrahlung photons. Figure 7.4 shows examples of EM showers in LAr in all three energy regimes. Shower length scales logarithmically with energy and generally propagates for a distance $\mathcal{O}(1)$ m for showers in the 10s of MeV to GeV range, while they are contained transversely by a Moliere radius of $\sim$9 cm.

Having highlighted the similarity between electron and photon propagation in LAr, it is worth mentioning the important differences that allow the LArTPC technology to distinguish between these two particles. Since photons do not carry electric charge, they do not deposit energy in LAr

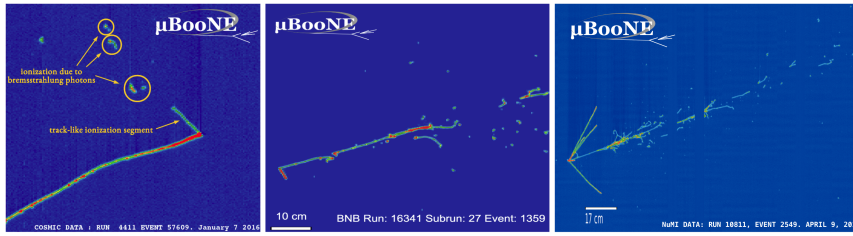


Figure 7.4. Examples of EM interactions in LAr. Left: Michel electron of several tens of MeV (reproduced from Ref. [27]). Center: Few hundred MeV EM showers from a $\nu_e$ interaction candidate (reproduced from Ref. [19]). Right: Higher energy EM shower from a $\nu_e$ interaction candidate (reproduced from microboone-exp.fnal.gov).

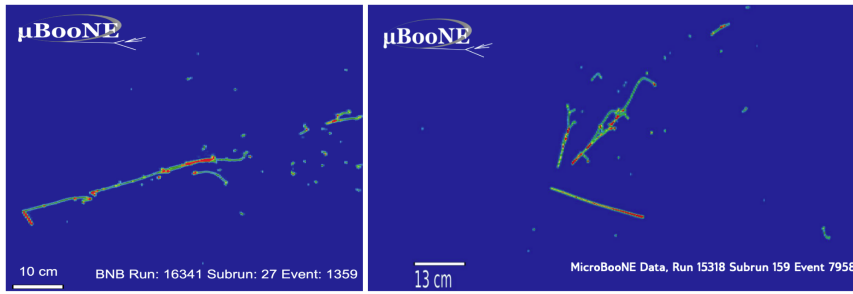


Figure 7.5. Left: Electron shower candidate from a $\nu_e$ interaction. Right: Two photon candidates from the decay of a $\pi^0$ produced in a neutrino interaction. In the event with photons, one can easily make out the gap from the shower start point to the interaction vertex (reproduced from microboone-exp.fnal.gov).

until they have interacted. The initial propagation distance covered by the photon before pair-converting leads to a visible "gap" from the neutrino interaction vertex. This gap is characteristic of photons' ∼20 cm conversion distance in LAr. Electrons, which ionize the argon as soon as they are produced, leave no such gap from their production point. Given the large conversion distance for photons, this gap is clearly visible in the detector but requires the presence of coincident activity at the interaction point such as visible tracks from the hadronic recoil. Figure 7.5 illustrates how the presence of a gap helps distinguish photons vs. electrons. The second distinguishing feature is associated with the energy loss profile at the start of the shower. The electron–positron pair produced by a photon will lead to double the ionization stopping power compared to a single electron. This difference will remain until the EM shower has a chance to develop, typically after several centimeters. The segment before the EM shower starts to fully

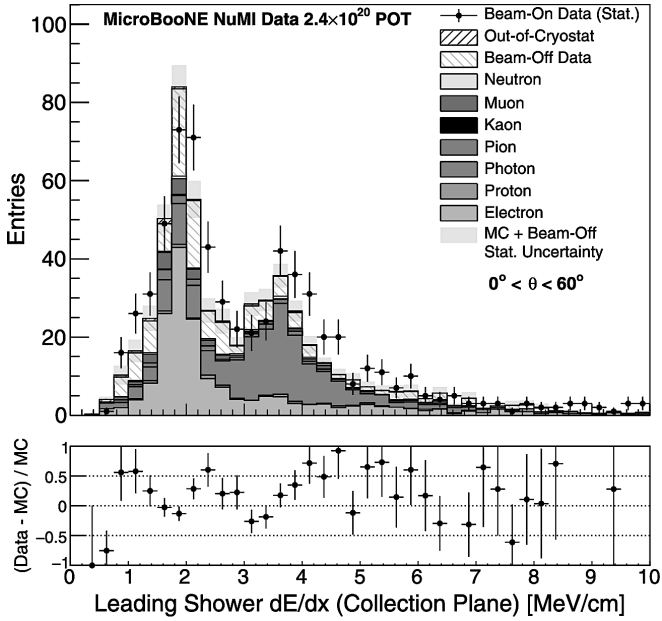


Figure 7.6. Distribution of shower trunk $dE/dx$ for electrons and photons observed in the MicroBooNE detector from the NuMI neutrino beamline. The distribution is dominated by electrons, in light gray, contributing at 2 MeV/cm, and photons, in dark gray, peaking at 4 MeV/cm.

*Source*: Figure reproduced from Ref. [28].

develop is referred to as the shower "trunk". Figure 7.6 shows one of the first demonstrations of this $e/\gamma$ separation technique, measuring the $dE/dx$ energy loss in the first four cm of the shower trunk and clearly distinguishing electrons, peaking at 2 MeV/cm from photons at twice that value.

#### 7.2.1.2 *Propagation of muons, charged pions, kaons, and protons*

Muons, charged pions, and protons do not radiate much of their energy at GeV energies. Instead, they primarily lose energy through direct ionization of the argon. This leads to "track-like" signatures: fairly linear segments of uniform ionization. Unless the particle re-interacts, it will come to a stop after having lost all its kinetic energy. The energy loss profile follows the Bethe–Bloch distribution, which describes the energy-dependent energy loss per unit distance ($\mathrm{d}E/\mathrm{d}x$) for a particle of a given mass. This

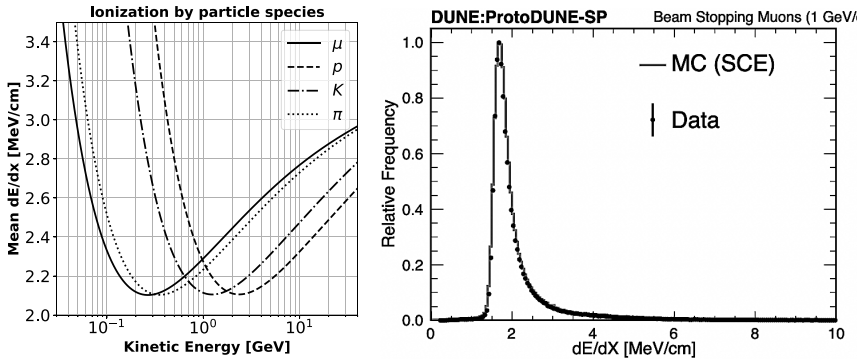


Figure 7.7. Left: Ionization energy loss for different particle species as a function of kinetic energy. Right: Measured dE/dx distribution from the protoDUNE detector for minimally ionizing muons.
*Source*: Figure from Ref. [10].

distribution is characterized by a minimum (occurring roughly when the particle's kinetic energy is equivalent to its mass) and a "Bragg peak": a sharp increase in the rate of ionization as the particle's energy decreases. Figure 7.7 shows the mean energy loss to ionization for muons, protons, charged pions, and kaons as a function of the particle's kinetic energy. While the Bethe–Bloch function describes the mean energy loss, the probability distribution function of the energy lost by a particle traversing a layer of argon follows a Landau–Vavilov distribution [29]. A useful metric by which ionization energy loss is quantified is the most probable value (MPV) of this distribution. Unlike the mean energy loss, the MPV depends on the thickness of the layer of material traversed, $dx$. Figure 7.7 (right) shows the distribution of $dE/dx$ measured with the protoDUNE detector with a sample of minimally ionizing muons, which have an MPV energy loss of roughly 1.7 MeV/cm.

While ionization is the primary means of energy loss for track-like particles, other interaction modes are relevant to the overall topology and energy loss profile in the TPC. Muons will occasionally produce $\delta$-rays: energetic electrons which branch out from the primary muon track. Protons and pions often reinteract with an argon nucleus before coming to rest, leading to more complicated topologies which can include a number of final state hadrons. These reinteractions are energy dependent, becoming more likely as the proton or pion's energy increases. Finally, muons, charged pions, and charged kaons will decay via the weak force once stopped,

each producing a characteristic signature in the detector. The decay chain differs depending on the charge of the particle. Positive muons will decay promptly to a Michel electron, while negatively charged muons will capture on argon and decay to an electron only ∼3/4 of the time. The resulting decay electron, referred to as a "Michel" electron, has an energy of up to half the muon mass and appears in the TPC as a secondary particle track branching from the muon end point (as can be seen in the left-most image of Fig. 7.4). When charged pions come to rest, they will decay promptly to a muon which subsequently follows the decay chain described above. The decay muon is produced with a small kinetic energy of $m_\pi - m_\mu \sim 35$ MeV, making it hard to detect and causing the pion-decay and muon-decay topologies to resemble each other. Finally, charged kaons can follow several possible decay modes. The most common (64% branching ratio) is to a muon and $\nu_\mu$. This decay path leads to a characteristic topology in the detector with a three-track segment of $K \to \mu \to e$ where the muon has a fixed energy of $m_K - m_\mu$ which can be leveraged for kaon identification.

#### 7.2.1.3 *Propagation of neutrons*

Neutrons are an important final-state particle in neutrino interactions yet are largely invisible in liquid argon. Their large interaction length often causes them to escape the detector entirely. This makes neutrons one of the main contributors to bias and uncertainty in neutrino energy reconstruction. When neutrons interact in the argon, they do so through neutron capture or inelastic scattering. Both processes lead to final-state low-energy photons, producing isolated point-like activity in the detector which rarely spans more than one wire on the TPC. These signatures can help determine the presence of neutrons but are not adequate for measuring their energy or direction. Higher energy inelastic scatters on argon can lead to final-state particles from the struck nucleus exiting with considerable energy, often producing visible protons. For the study of $\mathcal{O}(0.1 - 10)$ GeV neutrinos, the primary efforts tied to the measurement of neutrons are focused on identifying their presence in a neutrino interaction in order to improve neutrino energy reconstruction.

### 7.2.2 *Signal formation in LArTPCs*

As charged particles traverse the argon, their passage induces local perturbations to the electric field which transfer energy from the particle to electrons orbiting the argon nucleus. These electrons will either completely

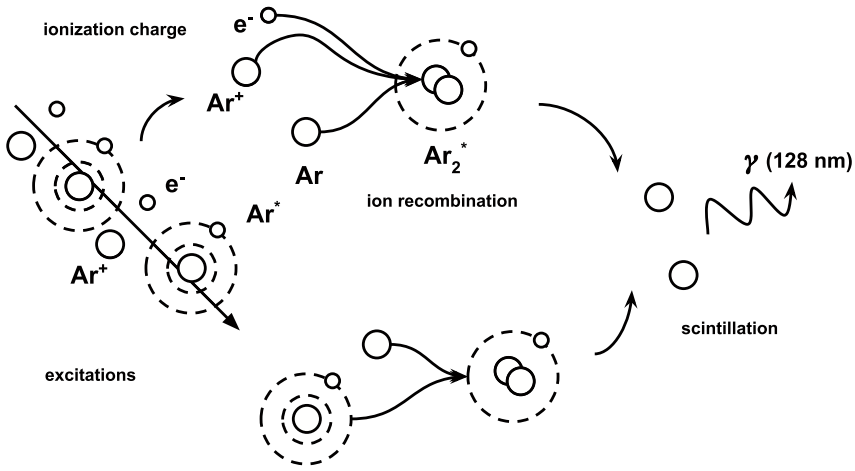


Figure 7.8. Ionization and excitation signal formation by the passage of a charged particle in liquid argon.

disassociate from the atom, leading to free electrons, or will reach a higher energy orbital, leading to an excitation which de-excites producing scintillation photons. One of the features which makes argon an ideal detector medium is the high yield for both signals, which are produced in roughly equal amounts. Roughly 40,000 scintillation photons and ionization electrons are liberated for every MeV of energy deposited. Figure 7.8 shows a schematic of the processes and ionization and excitation, and how these two paths are interconnected.

We describe the specific features of both signatures individually. Since the production of the two signatures is interconnected, we come back and discuss their interplay through the effect of ion recombination which influences particle identification and calorimetric measurements.

#### 7.2.2.1 *Ionization charge*

Ionization electrons are freed from their orbit as a consequence of the passage of a nearby energetic charged particle. The average energy expended per ion pair, referred to as $W$, determines the number of free electrons produced per amount of energy deposited. For liquid argon, this quantity is $23.6^{+0.5}_{-0.3}$ eV [30]. Given the $\sim$0.5 MeV of energy deposited by a particle on a single wire in a TPC, this leads to electron clouds of $\sim 10^4$ electrons drifting toward each wire. Ionization electrons produced in the

detector can have $\mathcal{O}$(eV) of energy but quickly thermalize to energies of a fraction of an eV as a consequence of random collisions with nearby argon atoms [31]. How these electrons behave next is complicated by the busy environment in which they find themselves: a sea of positive ($Ar^+$) and negative ($e$) ions which together cause an effect known as ion recombination, which is discussed in Section 7.2.2.3. The propagation of free electrons across the detector is discussed in Section 7.3.1.

#### 7.2.2.2 *Scintillation light*

Excited argon atoms rapidly combine with a ground-state argon atom to form excited dimer Rydberg states: an $Ar_2^*$ core with a bound, shared electron. Two different excitation states are populated, referred to as the "singlet" and "triplet", which get their name from how the spin of the electron and argon dimer are coupled. Both states de-excite to produce photons in the Visible Ultra-Violet (VUV) spectrum in a narrow wavelength range centered at 128 nm. The singlet and triplet excimers have significantly different lifetimes of 6 ns ("fast", or "prompt") and $\sim$1.3 $\mu$s ("late-light"), respectively, leading to two components in the scintillation light response. The ratio of scintillation photons produced via the singlet vs. triplet decay is roughly 1:3, though this ratio is dependent on the particle species and local electric field. The total light yield for scintillation light in argon is $\sim$40,000 $\gamma$/MeV [32], though again this quantity is dependent on the local environment and particle species, as become apparent in the following section describing ion recombination.

#### 7.2.2.3 *Ion recombination and impact on charge and light*

Ionization electrons are surrounded by their positively charged argon ion counterparts. The positive attraction between the $Ar^+$ and $e^-$ ions will cause them to recombine, an effect referred to as "ion recombination". The amount of electrons which will recombine with nearby positively charged ion atoms is a function of two key parameters: the local density of ions and the amount of time the electrons and $Ar^+$ are in close proximity. Ion density is proportional to the energy lost by the ionizing particle, $\mathrm{d}E/\mathrm{d}x$. How quickly ionization electrons will drift away from the positive ions instead depends on the strength of the external electric field $E$ applied in the TPC. Recombination, denoted as $\mathcal{R}$, is therefore expressed as a function of these two macroscopic observables, $\mathcal{R}(dE/dx, E)$.

Ion recombination has two key consequences for LArTPC particle detection. First, ion recombination leads to a nonlinear relation between deposited energy and observable charge. This is due to the larger amount of recombination (and therefore larger fractional charge quenching) which takes place for larger local energy deposition, where a higher density of ions leads to an increased probability of electrons recombining. The second key impact is to closely link ionization and scintillation signatures. As electrons recombine with positively charged ions, they do so forming excited states which in turn produce scintillation photons. The charge quenching caused by recombination thus leads to an increase in scintillation light. This leads to an anti-correlation between the yield of ionization electrons and scintillation photons. For a sense of scale, minimally ionizing muons ($dE/dx \sim 2.1$ MeV/cm) observe charge quenching of 30–50%, while for highly ionizing particles such as protons in the Bragg peak, the amount of charge quenching can reach 80% or more. Two detailed studies and most widely used parametrizations for ion recombination were produced by the ICARUS [33] and ArgoNeuT [34] experiments.

## 7.3 LArTPC Signal Propagation

Argon is transparent to its own scintillation light and ionization charge, making it an excellent detector target for signal transport over the large volumes necessary to observe neutrino interactions with high statistics. Ionization charge drifts uniformly under the influence of the TPC's electric field producing a 3D map which faithfully tracks the trajectory of charged particles in the detector, while scintillation photons propagate isotropically from their point of origin. This section focuses on describing the details of how ionization electrons and scintillation photons propagate through the argon to reach their respective sensors.

### 7.3.1 *Ionization charge transport*

Once ionized, electrons begin to drift under the influence of the external TPC electric field. While this causes electrons to accelerate in the direction opposite the electric field, the intrinsic thermal motion of the electrons, and their constant collision with nearby argon atoms, leads them to quickly reach terminal velocity and drift at a uniform speed. The drift velocity grows logarithmically with increasing $E$-field strength. The relatively slow drift velocity causes ionization charge to take $\mathcal{O}$ (ms) to drift over $\mathcal{O}$ (m)

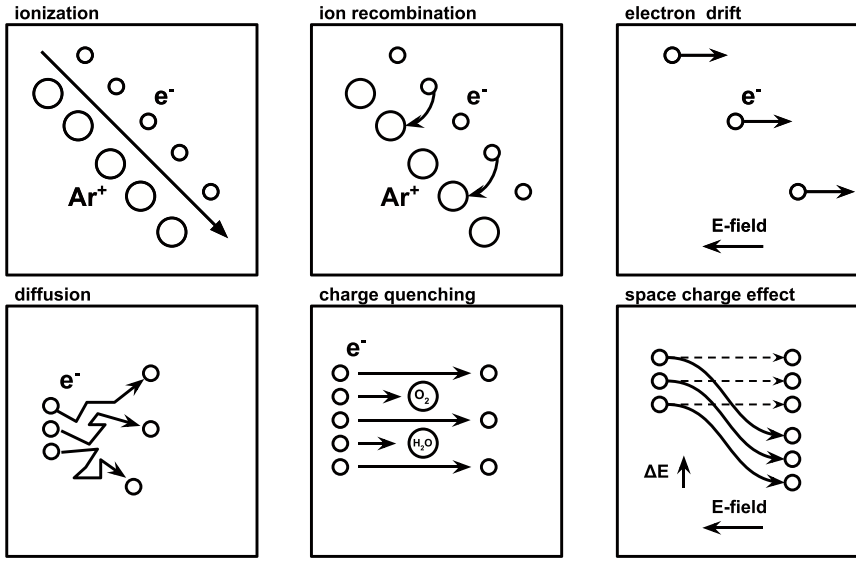


Figure 7.9. Detector effects that impact the propagation and transport of ionization charge across the TPC.

scales. This has significant impact on the design of electronics and DAQ systems which must record charge from the TPC for this timescale to fully image interactions and can lead to pile-up of interactions, such as coincident cosmic rays. During this relatively slow journey across the detector, several factors can interfere with the propagation of free electrons. Quenching due to electronegative impurities, diffusion of ionization clouds, and distortions due to "Space-Charge" effects are all described next. Figure 7.9 illustrates the detector effects that impact the propagation and transport of ionization charge across the TPC.

#### 7.3.1.1 *Charge quenching due to impurities*

Electronegative impurities in the argon attract the drifting electrons, quenching the charge signal. The rate at which electrons are absorbed is directly proportional to the impurity concentration. Water and oxygen, natural contaminants in argon, are the primary contributors to charge quenching. With concentrations at the part-per-billion (ppb) level, the attenuation length of ionization electrons becomes of order meters. Limiting the amount of impurities in the argon is therefore essential in order to operate LArTPC detectors with meter-scale drift lengths. Achieving high

argon purity was one of the key technological developments that has enabled the LArTPC technology to mature into a viable detection method for neutrino experiments. Charge quenching leads to a non-uniform detector response, due to the exponential suppression of ionization charge as a function of depth in the TPC (along the direction of the TPC's electric field). If impurity concentrations are too high, charge signals will fade away and not be detected on the TPC wires. Significant effort has gone into achieving high-purity through advances in engineering of the cryogenic recirculation and purification systems for LArTPC. Figure 7.10 from Ref. [35] shows the measured water and oxygen concentration in the MicroBooNE cryostat during detector commissioning as a function of time after initiating argon filtration. While water and oxygen have the largest impact due to their relatively larger concentrations, other contaminants can quench argon signals. A review and assessment of the impact on electron attenuation due to different contaminants can be found in Ref. [36].

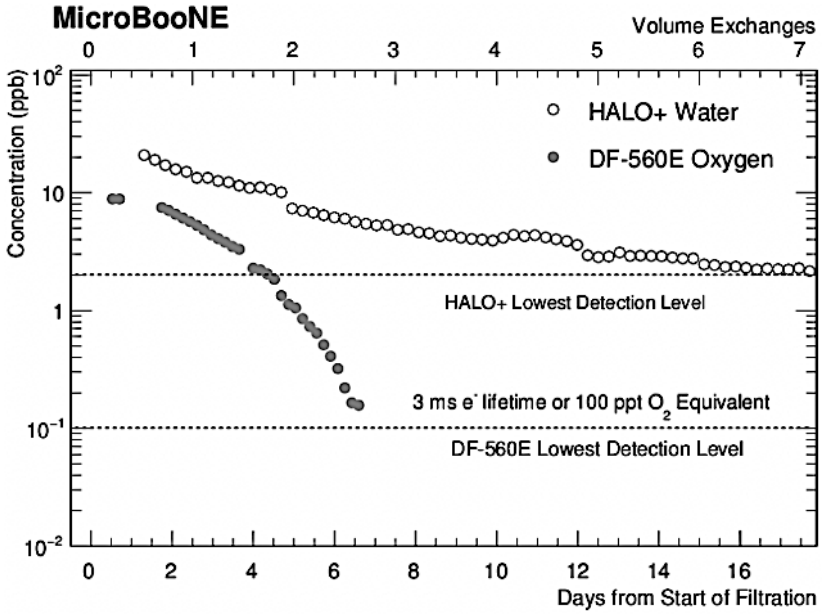


Figure 7.10. Concentration of water and oxygen in the MicroBooNE cryostat as a function of days since filtration of the argon. The detector reaches concentrations at or below one part per billion, enabling high electron lifetime and therefore high signal transparency across the TPC volume.

*Source*: Figure from Ref. [35].

#### 7.3.1.2 *Ion diffusion*

The collisions occurring on a microscopic scale between drifting electrons and argon atoms lead to a broadening of the electron clouds produced by ionization. Diffusion affects aspects of detector performance tied to position resolution, peak amplitude (impacting detection thresholds), and the optimization of aspects of TPC readout, such as sampling frequency and electronics shaping response. Furthermore, diffusion can affect calculations of charge-sharing across TPC wires [37, 38], impacting calibrations. Macroscopically, diffusion leads to the broadening of electron clouds of one micron after a propagating over a drift distance of 1 m. The exact magnitude is different in the component along the direction of the electron drift (longitudinal, $D_L$) and that perpendicular to it (transverse, $D_T$) and is impacted by the strength of the local electric field. Diffusion is quantified as the spread in an electron cloud in $\text{cm}^2/\text{s}$. Measurements are typically performed for $D_L$, with values in the 4–6 $\text{cm}^2/\text{s}$ range [39–41]. Values of the transverse diffusion $D_T$ are typically slightly larger and also depend on the value of the local electric field.

#### 7.3.1.3 *Space charge effect*

Positive argon ions drift as well, though much more slowly than their electron counterparts. In surface LArTPCs, a large steady-state rate of ionization from cosmic rays leads to a build-up of positively charged Ar ions in the detector, which in turn distorts the electric field in the TPC, causing what is referred to as the space charge effect (SCE). SCE in a TPC has the same effect as atmospheric aberration for telescopes: by causing local distortions in the TPC's uniform electric field, it bends the otherwise straight trajectory of drifting electrons. Uncorrected, it leads to a distortion of the reconstructed 3D charge map for ionization taking place in the TPC. Figure 7.11 shows the impact of this effect in the MicroBooNE detector: dotted lines represent the actual detector boundaries in the drift ($x$) and vertical ($y$) coordinates, while the scatter points are the start and endpoint of reconstructed cosmic-ray tracks in the detector before any SCE corrections are applied. The large differences between the two, particularly close to the cathode plane (right boundary in the figure), are a consequence of the deflection of ionization drift due to positive ions.

Positively charged ions tend to build up near the TPC cathode, where distortions are greatest. The varying electric field further impacts detector response by impacting the amount of ion recombination (see Section 7.2.2.3)

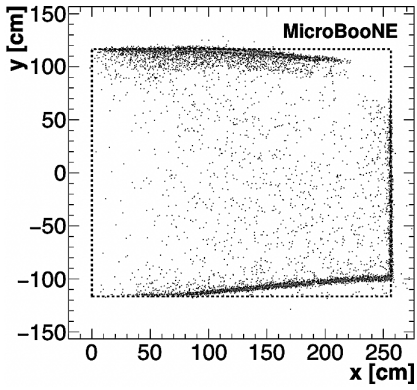


Figure 7.11. Effect of SCE as seen in MicroBooNE.
*Source*: Figure from Ref. [42].

and therefore the charge and light yield. The magnitudes of SCE distortions are both dependent on the position within the detector and on the rate of positive ion build-up in the detector. This second quantity depends primarily on the steady-state rate of ionizing radiation to which the detector is exposed: more ionization leads to a larger SCE effect. This means that detectors operating on the surface will be impacted by a significantly larger SCE effect than those underground. Quantitative studies of SCE effects have been carried out with the ICARUS [43], MicroBooNE [42, 44], and protoDUNE [10] detectors. What is a macroscopic offset of $\mathcal{O}$(1-10) cm on the surface becomes a negligible effect underground, where the cosmic-ray rate is suppressed by several orders of magnitude.

### 7.3.2 *Scintillation light propagation*

The fact that argon is transparent to its own 128 nm scintillation photons means that to first-order photons collected as a function of distance from the production point follow a $1/r^2$ dependence. Rayleigh scattering and attenuation due to impurities impact the total amount of light collected and cause to deviate from this relationship. These two effects are described next.

#### 7.3.2.1 *Rayleigh scattering*

Rayleigh scattering describes elastic scattering of light on particles of wavelength smaller than that of the incident photon. The Rayleigh

scattering rate is proportional to $1/\lambda^4$ and therefore has a strong dependence on the photon wavelength. Recent measurements [10, 45] of the Rayleigh scattering length on argon report a value of ∼90–100 cm. These measurements are complicated by the fact that detector volumes for existing LArTPCs are of similar scale to the scattering length itself, and numerous effects can contribute to impacts that mimic that of scattering. The primary impact Rayleigh scattering has on detecting scintillation photons is to modify the simple $1/r^2$ dependence expected on the number of photons observed as a function of distance and direction from their production location. Rayleigh scattering also directly impacts the group velocity of photons traveling in argon, with a measured value from Ref. [45] of $13.4 \pm 0.1$ cm/ns. In this context, doping of argon with Xenon has been proposed as a way to mitigate the impact of Rayleigh scattering over large volumes due to the larger emission wavelength of ∼178 nm for xenon.

#### 7.3.2.2 *Light attenuation*

Impurities in the argon can quench scintillation photons. Nitrogen, a contaminant found at the part-per-million level, has the largest impact, quenching scintillation light by "stealing" the shared electron from excited argon dimers. The very fast decay timescale of the singlet state leaves it almost completely unaffected by nitrogen contaminants, which instead compete with the de-excitation of the longer-lived (1.3 $\mu$s) triplet state. Quenching of the triplet excited state causes, in addition to an overall decreased light yield, a reduction of the effective late-light time constant. This in turns impacts the use of scintillation light for pulse-shape discrimination and other application of timing obtained from scintillation light.

## 7.4 LArTPC Signal Detection

Once drifting electrons and scintillation photons have reached the edges of the detector, they are detected by charge and light sensors, respectively. In this section, we describe the methods and hardware used to record these two signatures.

### 7.4.1 *Ionization charge detection*

The method employed to measure the ionization signature of an LArTPC traditionally relies on wire sensors. More recently, pixel-based detectors have been proposed and successfully operated. We discuss largely

wire-based readout, which has been used in LArTPC detectors for many decades. While the core detection principle is the same, details tied to hardware and operations of pixel-based detectors can be found in Refs. [46, 47].

A wire-based TPC must be able to produce multiple signatures for the same cloud of ionization electrons on different wire planes in order to recover the 3D position of the energy deposition. To achieve this, wires are arranged in distinct planes at different orientations. Each plane is operated at a specific voltage in order to allow clouds of electrons to drift past the first wire planes, while still inducing a detectable signal, finally causing the charge to collect on the last, "collection" plane. The left panel of Fig. 7.12 shows a top-down view of the MicroBooNE detector with different wires denoted as dots arranged on three planes. The field lines followed by ionization electrons converge on the bottom (collection) plane. The image on the right shows the induced signature (top and middle) and collected charge (bottom) caused by the same cloud of ionization electrons. The time-coincidence of these signals, together with knowledge of the geometric location of the wires, allows us to recover the 3D coordinates of the energy deposited. The need for distinct wire planes comes with significant design challenges tied to achieving full transparency through the application of appropriate bias voltages on the three wire planes. This in turn motivates a

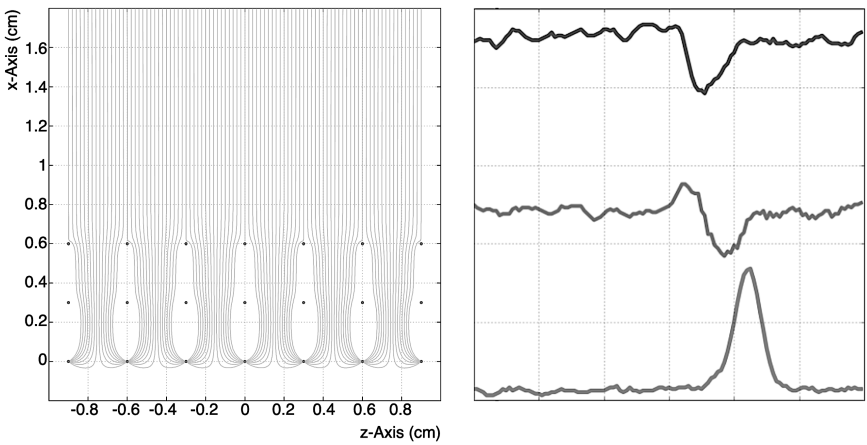


Figure 7.12. Wire geometry and simulated trajectory of drifting electrons for the MicroBooNE TPC wire plane.

*Source*: Figure from Ref. [48].

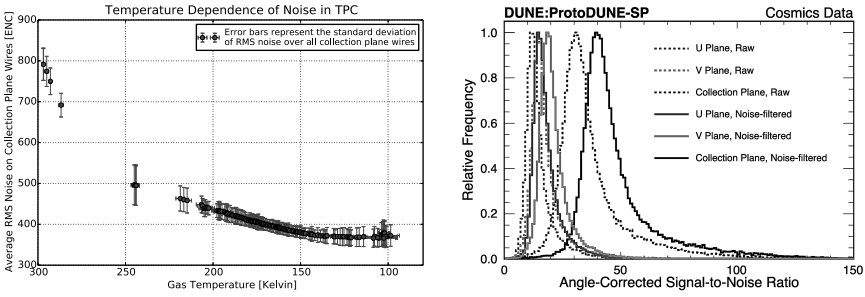


Figure 7.13. Left: Temperature dependence of TPC noise with cold electronics from MicroBooNE [51]. Right: Signal-to-noise measured in protoDUNE data [11].

detailed understanding of the field response which causes the induced and collected signals. Extensive details on this topic are provided in references on TPC signal processing from the MicroBooNE collaboration [48, 49].

The ability to effectively operate the TPC depends on achieving sufficient signal-to-noise to detect drift electrons. The development of low-power cold electronics for TPC wire readout [50] have enabled further noise suppression that has brought noise levels in TPCs to the few-hundred electrons in Equivalent Noise Charge (ENC). Figure 7.13 (left) shows the noise dependence on temperature for MicroBooNE's TPC collection plane wires, indicating the significant reduction at LAr temperatures. The right panel of Fig. 7.13 shows the signal-to-noise for ionization in protoDUNE measured on all three wire-planes. Signal-to-noise levels of ∼40 are achieved for minimally ionizing muons on the collection plane.

### 7.4.2 *Scintillation light detection*

Detecting scintillation light photons produced in argon requires being sensitive to their 128 nm wavelength. Wavelength shifters are used to convert the 128 nm photons to photons of longer wavelength which can be detected by PMTs or SiPMs. TetraPhenyl-Butadiene (TPB) is an organic scintillator molecule which efficiently absorbs VUV photons re-emitting them with a wavelength of ∼400–500 nm, a range that allows them to penetrate the glass surrounding a PMT and undergo photoelectric conversion on the photocathode. Other wavelength shifters are also available, and a review of LAr scintillation light wavelength shifters is available in Ref. [52]. Integrating the TPB wavelength shifter in LAr detector design has been achieved through multiple methods, including coating directly the PMT's

glass surface, placing a TPB-coated plate directly in front of the PMT [8], or coating the detector surface [53]. In coincidence with development of PD systems for the DUNE experiments, further solutions for LAr scintillation detection have been designed. In particular, the ARAPUCA [54,55] concept acts as a light trap through the use of a dichroic filter and leads to two wavelength shifting stages: the first to allow photons to enter the detector and the second to trap them in the scintillator strip. Since the ARAPUCA concept was introduced, this detector technology has expanded in several directions and is being deployed in detectors such as protoDUNE [10] SBND, and the DUNE Vertical Drift technology [56]. Increasing the light yield is also achieved through the installation of wavelength-shifting and/or reflective surfaces on the inner walls of the TPC. This solution was employed by the WarP [53] detector and is being implemented in the SBND TPC, where it will provide high light yield of $\mathcal{O}(100)$ PE/MeV uniformly across the TPC volume, countering the $1/r^2$ dependence typically seen for scintillation signals due to the asymmetric positioning of light sensors in the cryostat.

### 7.4.3 *Auxiliary detectors*

LArTPC detectors are sometimes accompanied by external Cosmic Ray Taggers (CRTs) which consist of scintillator strips mounted externally to the detector's cryostat and are leveraged to identify coincident cosmic-ray particles which traverse the detector volume. CRTs such as those described in Refs. [57, 58] are primarily used to form anti-coincidences for vetoing cosmic-ray activity that may mimic neutrino interactions.

## 7.5 Operation, Performance, and Calibration of Liquid Argon Neutrino Detectors

Achieving stable operation of large-scale LArTPC detectors has been a major technological milestone that has enabled the technology to produce high-quality physics results and set the stage for decade-long operation of detectors, such as DUNE. A significant component of LArTPC operations is the need to operate a reliable cryogenic infrastructure to circulate, replenish, and purity the LAr inside the detector cryostat. While not discussed in this chapter, Refs. [5, 8, 23, 59] provide valuable information on the topic.

One of the advantages of the LArTPC technology is the ability to not only image particle interactions with high resolution but also provide the

detailed calorimetry necessary for quantitative measurements of particle kinematics. For modern experiments, this inevitably requires having access to efficient and accurate reconstruction and calibration techniques which are able to process and interpret data in an automated way, providing reconstructed particle kinematics on an event-by-event basis to be used to develop event selections and carry out physics measurements. This is particularly true for neutrino experiments which aim to study complex particle interactions where the final-state observables vary both in particle species and kinematics. Having established the successful operation of LArTPC detectors and their ability to collect rich datasets of neutrino interactions, it is important to discuss the technological challenge of leveraging these data for precise neutrino measurements with sophisticated pattern recognition and analysis tools. Furthermore, it is worth highlighting the significant progress made in recent developments in reconstruction and analysis methods for LArTPC detectors. Due to these reasons, we dedicate this section to reviewing the status and progress in the calibration and analysis of LArTPC datasets.

### 7.5.1 *LArTPC reconstruction*

Converting the raw signals obtained from an LAr neutrino detector into quantitative measurements of particle kinematics for use in physics analyses is a task that falls under the name of "event reconstruction". This is a fundamental operation without which the quality of the data obtained from the detector cannot be put to use for quantitative physics measurements. This operation needs to be performed in an automated way, through computing tools that can be run at-scale over millions of events and are reproducible. Significant progress has been made to deliver high-quality reconstruction methods for LArTPC detectors. Contributions from the ICARUS, ArgoNeuT, MicroBooNE, and protoDUNE experiments have, in different phases, spearheaded the publication of physics results with LArTPC data. We briefly discuss the major components in LArTPC event reconstruction for LArTPC detectors.

#### 7.5.1.1 *Signal processing and hit finding*

Converting signals recorded on individual wires (or pixels for pixel-based LArTPC detectors) into measurements of charge deposition is the first step in most reconstruction workflows. This operation takes several forms but often starts with an initial signal processing stage which is responsible

for filtering TPC electronics noise and applying signal deconvolution to correct for the impact of electronics response on signals induced by drifting electrons. The outcome of this process is a measurement of the amount and arrival time of charge for each recorded energy deposit on a wire. While these tasks are not new to LArTPC reconstruction, they have been significantly expanded in recent years. Reference [60] discusses the noise-filtering techniques utilized both in hardware and offline analysis, which lead to achieving signal-to-noise of up to 50-to-1 on the collection plane. References [48, 49] describe the signal processing developed to reconstruct signals from raw waveforms. Of note is the innovative 2D deconvolution methods implemented to account for angle-dependence in wire response and the impact of charge-sharing across wires, which when incorporated in the deconvolution procedure provide a more uniform detector response and higher signal efficiency for tracks oriented with a large pitch with respect to the wire plane. Figure 7.14 shows the impact of 2D deconvolution on

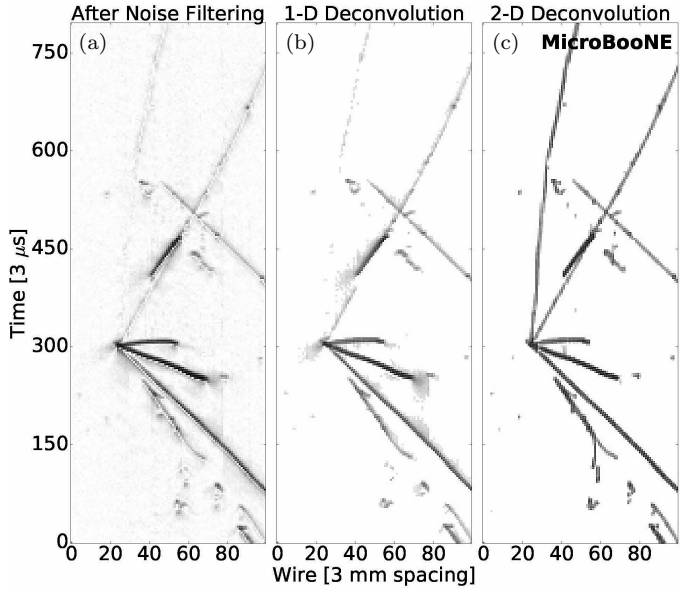


Figure 7.14. Two-dimensional deconvolution applied to a MicroBooNE neutrino interaction candidate. The sharpness of the tracks originating from the neutrino interaction vertex (at coordinates 20 mm, 300 $\mu$s) is significantly improved in the 2D deconvolution method (right panel) with respect to a 1D approach (center). This can be seen clearly in the tracks that are aligned with the vertical coordinate in the image.

*Source*: Figure from Ref. [48].

signal from a neutrino interaction candidate recorded with the MicroBooNE LArTPC. Charge measurements on each plane, often referred to as "hits", need to then be correlated across planes to produce 3D patterns of energy deposition. This is achieved by relying on the geometric overlap of wire planes and charge-matching deposits of equal charge on different wire planes. Different reconstruction paradigms perform the transition from 2D to 3D differently, and several workflows which employ image-like pattern recognition through machine learning techniques rely directly on wire images as input to tracking and PID algorithms.

#### 7.5.1.2 *Tracking and particle flow reconstruction*

Given the measured energy deposits in the TPC, reconstruction algorithms are next tasked with isolating individual interactions taking place in the detector. For surface detectors, where the large rate of external cosmic-ray interactions leads to "busy" events, this can be a fairly complex task. An example event from the MicroBooNE detector is shown in Fig. 7.15, where dozens of cosmic-ray interactions pile up on top of a single neutrino interaction, shown in the zoomed in panel. The image gives a sense of the reconstruction complexity involved. The individual particles making up each interaction need to be isolated and tracked. These tasks are

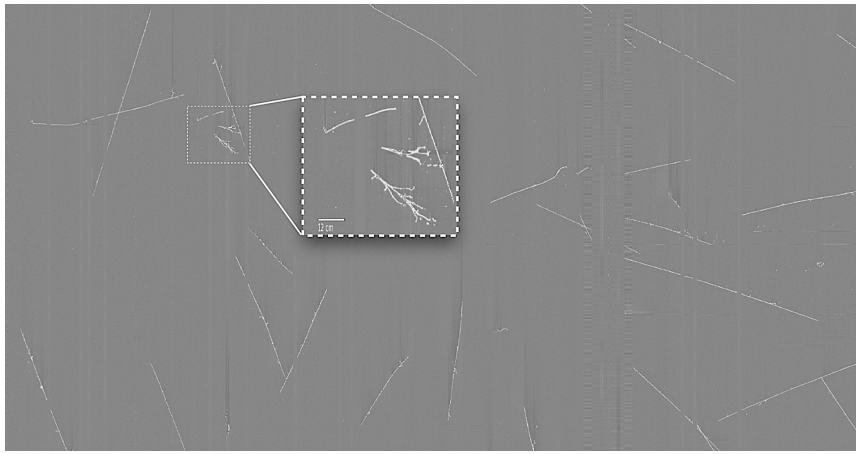

Figure 7.15. Collection-plane view of an event recorded by MicroBooNE. The event is filled with cosmic-ray interactions which reach the detector during the TPC's $\mathcal{O}$(ms) drift window. The single beam neutrino interaction in the event is isolated in the zoom-in panel.

achieved through the employment of multi-algorithm chains which leverage the position and charge map of energy deposits to identify particle tracks and their parentage relationship. Comprehensive reconstruction toolkits such as Pandora [61, 62] and Wire-Cell [63, 64] offer fully automated reconstruction with tracking and particle-flow reconstruction for generic neutrino and cosmic-ray interactions. Machine learning techniques have also been developed to leverage the image-like quality of LArTPC data for the purpose of event reconstruction. Details on such methods are documented in Refs. [65–71].

#### 7.5.1.3 *Cosmic rejection and charge-to-light matching*

Surface LArTPC detectors suffer from a high rate of cosmic-ray activity which swamps neutrino signals, in part due to the slow TPC readout. Even for events where a neutrino interaction occurs in the detector, $\mathcal{O}(10)$ cosmic-ray interactions pile-up on the neutrino image, requiring tools that are capable of identifying and isolating the TPC charge deposited by the neutrino interaction. This task is referred to as "flash-matching", or "charge-to-light" matching. Leveraging the prompt scintillation light-signature in-time with the beam, flash-matching identifies the interaction in the TPC that is compatible with the observed scintillation light signal. This is achieved by comparing the geometric pattern of scintillation light recorded in the detector to the light that is predicted to hit each photosensor based on the spatial charge distribution. This matching leverages the absolute charge and position-dependence collected with both the PDS and TPC systems and is capable of reducing cosmic-ray backgrounds from signal-to-background levels of 1 : 100 to 1 : 1 or better [72, 73]. Figure 7.16 shows how this operation takes place. The left panel shows a side view of the MicroBooNE TPC with the PMT positions denoted by circles. The

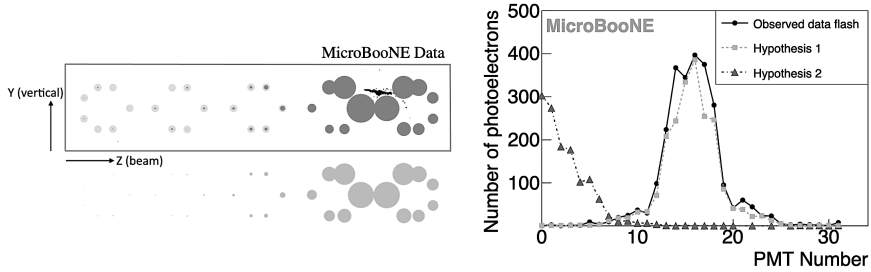


Figure 7.16. Flash matching illustrations from Refs. [72, 73].

elongated splash in the image is a candidate $\nu_e$ interaction reconstructed with TPC information. The circles within the TPC rectangle indicate the number of photoelectrons recorded by the PMT array in-time with the neutrino beam, while the circles below the TPC represent the expected light predicted based on the observed charge recorded by the TPC. The good match between them indicates that the TPC interaction is consistent with having occurred in-time with the beam. The image on the right shows an analogous quantitative study comparing the spectrum of photoelectrons recorded on the PMT array (solid line) to the predicted number of photons based on the pattern of charge from two different TPC interactions: one of them clearly matches, while the other can be rejected.

#### 7.5.1.4 *Calorimetry, particle kinematics measurements, and particle ID*

Once individual particle tracks are reconstructed in the TPC, their kinematics (momentum and direction) and particle species are reconstructed leveraging the TPC's spatial and calorimetric information. Particle ID first aims to determine the track-like or shower-like nature, which typically separates track-like $\mu$, $p$, $\pi^{+/-}$, and $K$ from shower-like $e$ and $\gamma$ particles. Within track-like particles, calorimetric PID algorithms make use of the $dE/dx$ vs. residual range profile characteristic of each particle to determine the particle species. Figure 7.17 shows the characteristic separation in energy-loss profile for protons and muons. For contained tracks, compatibility with the expectation for each particle species (given by the solid theoretical lines superimposed on the figure) allows us to provide accurate PID. Electron–photon separation is a task that was introduced in Section 7.2.1.1 and leverages two key features: the "gap" between an interaction vertex (when visible) and the start of the EM shower which is present for photons but not for electrons, and the energy loss at the shower trunk, which for photons which pair convert is twice as large as for electron showers. Figure 7.6 shows an example of this second, calorimetric classification method.

While LArTPCs provides excellent PID capabilities, charge sign determination is a task that is not performed on a particle-by-particle basis in LArTPCs given the lack of an external magnetic field.

Once the particle species is determined, a measurement of its kinematics follows. For track-like particles (muons, protons, and pions) which come to stop in the detector, their momentum is typically estimated by range,

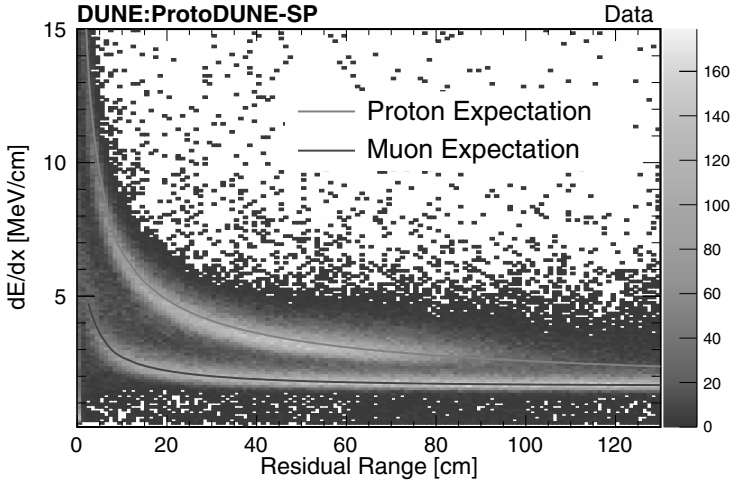


Figure 7.17. Muon and proton $dE/dx$ profile vs. residual range from protoDUNE [10]. The grayscale histogram shows measured energy loss as a function of residual range for proton and muon candidates. The population with larger $dE/dx$ values is associated with protons which ionize more heavily. The difference in energy loss profile between different particle species allows for precise particle ID in LArTPC detectors.

leveraging the strong correlation between track length and momentum. This method gives an energy resolution of a few percent for protons and muons. While the method works well for charged pions as well, their higher probability of re-interacting makes a momentum determination more difficult to obtain reliably. The effect of Multiple Coulomb Scattering (MCS) is used for energy estimation for uncontained muons. MCS leverages the correlation between a muon's energy and the average angular deflection due to Coulomb scattering to measure the muon energy with an accuracy of ∼20%. This method, employed through the use of a likelihood and demonstrated in both the ICARUS [74] and MicroBooNE [75] experiments, proves reliable up to $\mathcal{O}(1)$ GeV energies, at which point the scattering amplitudes become comparable with the detector's angular resolution. For EM showers from electrons and photons, energy reconstruction is calculated calorimetrically by integrating the visible charge deposited in the TPC. This method, which requires careful considerations tied to absolute energy scale calibration, including the impact of ion recombination on EM showers, achieves performance which ranges in the 10–20% resolution. Importantly, the method is often limited by reconstruction inefficiencies in fully collecting charge produced by the EM shower which either falls below

hit-reconstruction thresholds or is incorrectly missed by charge-clustering algorithms. This inefficiency also leads to a need for corrections to any potential bias in determining the shower energy, which lead to an underestimation of the shower energy if left uncorrected. Extensive details on EM shower energy-scale reconstruction and calibrations can be found in Refs. [27, 76–79].

#### 7.5.1.5 *Machine learning in LArTPC reconstruction*

Machine Learning (ML) and Artificial Intelligence (AI) have become integral components of data analysis in high energy physics. The development of reconstruction tools based on ML methods has in particular leveraged the image-like features of LArTPC datasets. These methods often rely on the use of deep or sparse neural networks which have found broad application in AI and computing beyond physics. Tasks such as neutrino identification [80,81], pixel-based particle ID [82,83], and reconstruction [84] are all rapidly making significant advances in reconstruction capabilities and being deployed in physics measurements [20].

### 7.5.2 *Detector calibrations*

Calibrating for the multiple effects which impact charge and light signals described earlier in this chapter requires significant effort. Several strategies and sources are leveraged to perform calibrations of different signals. Intrinsic sources of energy loss provide valuable samples for detector calibration. In particular, surface LArTPCs can leverage a uniform and steady-state rate of cosmic-ray muons for relative position-dependent and absolute energy-scale calibrations. Samples of both neutrino and cosmic-ray induced particles often leveraged include $\pi^0 \to \gamma\gamma$ decays and Michel electrons for EM shower energy-scale calibrations, as well as stopping protons and muons for absolute energy-scale and ion recombination calibrations. Figure 7.18 shows the reconstructed invariant mass from diphotons coming from $\pi^0$ candidates. The kinematics of the $\pi^0$ decay allow us to recover the $\pi^0$ mass and provide a valuable way to validate and calibrate EM shower energy-scale reconstruction.

In addition to this "free" calibration source, several detector subsystems and components are installed to provide additional tools intended to meet particular calibration challenges. Ionizing lasers such as that described in Ref. [85], which produce continuous track-like segments of ionization in the TPC, are used to map out the electric field in the TPC and calibrate

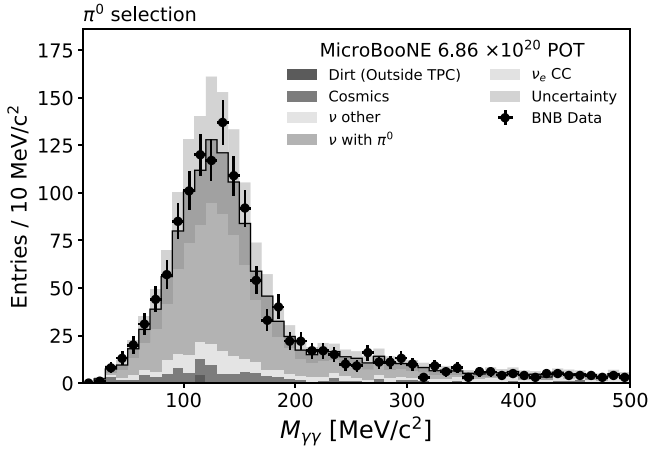


Figure 7.18. Reconstructed invariant diphoton mass from $\pi^0$ candidates.
*Source*: Figure from MicroBooNE [19].

effects such as SCE. Scintillation light LED calibration systems such as those described in Refs. [10, 86] also help complement natural sources of photons.

Calibrations for scintillation light signatures have been developed by several experimental collaborations leveraging either test-beam facilities (protoDUNE [11] and LArIAT [87]) or leveraging cosmogenic muons and protons as in the case of MicroBooNE [88, 89].

Calibration of the TPC response to ionization is critical in order to obtain accurate calorimetric measurements necessary for PID and particle kinematics measurements. Calibrations that cover relative distortions in the charge response across the TPC volume need to account for multiple effects, including dependence on the local wire response, quenching due to impurities, and SCE distortions. Absolute energy-scale calibrations responsible for converting measured currents on the wires into total energy deposited are instead primarily impacted by electronics gain and ion recombination. While multiple calibration techniques are employed to measure each effect independently, they are often integrated in a comprehensive calibration strategy, described in Ref. [90] for the MicroBooNE experiment and Ref. [10] for protoDUNE. A comprehensive review of these methods is presented in Ref. [91]. The calibration of EM showers poses specific challenges tied to the topology of shower propagation in liquid argon. This is in part due to the lossy nature of EM shower energy reconstruction, which relies on

calorimetric charge measurements but may suffer from charge falling below threshold or reconstruction inefficiencies. The importance of EM shower energy-scale calibrations is paramount to both the $\nu$ oscillation program searching for $\nu_\mu \to \nu_e$ signatures with electron showers in the final state as well as BSM searches in the sub-GeV regime which often include EM shower final states. The topic of EM shower calibrations in LArTPCs is discussed in several articles, including Refs. [27, 76–79].

## References

[1] W. J. Willis and V. Radeka. Liquid argon ionization chambers as total absorption detectors. *Nuclear Instruments and Methods in Physics Research Section A: Accelerators, Spectrometers, Detectors and Associated Equipment*, 120:221–236, 1974.

[2] D. R. Nygren. The time projection chamber: A new 4 pi detector for charged particles. *eConf*, C740805:58, 1974.

[3] C. Rubbia. The liquid argon time projection chamber: A new concept for neutrino detectors, May 1977.

[4] H. H. Chen, P. E. Condon, B. C. Barish, and F. J. Sciulli. A neutrino detector sensitive to rare processes. I. A study of neutrino electron reactions, May 1976.

[5] P. Cennini, *et al.* Performance of a 3-ton liquid argon time projection chamber. *Nuclear Instruments and Methods in Physics Research Section A: Accelerators, Spectrometers, Detectors and Associated Equipment*, 345:230–243, 1994.

[6] S. Amerio, *et al.* Design, construction and tests of the ICARUS T600 detector. *Nuclear Instruments and Methods in Physics Research Section A: Accelerators, Spectrometers, Detectors and Associated Equipment*, 527:329–410, 2004.

[7] P. Abratenko, *et al.* ICARUS at the Fermilab short-baseline neutrino program: Initial operation. *The European Physical Journal C*, 83(6):467, 2023.

[8] R. Acciarri, *et al.* Design and construction of the MicroBooNE detector. *JINST*, 12(02):P02017, 2017.

[9] R. Acciarri, *et al.* The liquid argon in a Testbeam (LArIAT) experiment. *JINST*, 15(04):P04026, 2020.

[10] B. Abi, *et al.* First results on ProtoDUNE-SP liquid argon time projection chamber performance from a beam test at the CERN neutrino platform. *JINST*, 15(12):P12004, 2020.

[11] A. Abed Abud, *et al.* Design, construction and operation of the ProtoDUNE-SP liquid argon TPC. *JINST*, 17(01):P01005, 2022.

[12] M. Antonello, *et al.* A proposal for a three detector short-baseline neutrino oscillation program in the Fermilab booster neutrino beam, March 2015.

[13] P. A. N. Machado, O. Palamara, and D. W. Schmitz. The short-baseline neutrino program at Fermilab. *Annual Review of Nuclear and Particle Science*, 69:363–387, 2019.

[14] B. Abi, *et al.* Long-baseline neutrino oscillation physics potential of the DUNE experiment. *European Physical Journal C*, 80(10):978, 2020.

[15] B. Abi, *et al.* Supernova neutrino burst detection with the deep underground neutrino experiment. *European Physical Journal C*, 81(5):423, 2021.

[16] B. Abi, *et al.* Prospects for beyond the standard model physics searches at the deep underground neutrino experiment. *European Physical Journal C*, 81(4):322, 2021.

[17] P. Abratenko, *et al.* Search for an excess of electron neutrino interactions in MicroBooNE using multiple final-state topologies. *Physical Review Letters*, 128(24):241801, 2022.

[18] P. Abratenko, *et al.* Search for neutrino-induced neutral-current $\Delta$ radiative decay in MicroBooNE and a first test of the MiniBooNE low energy excess under a single-photon hypothesis. *Physical Review Letters*, 128:111801, 2022.

[19] P. Abratenko, *et al.* Search for an anomalous excess of charged-current $\nu$e interactions without pions in the final state with the MicroBooNE experiment. *Physical Review D*, 105(11):112004, 2022.

[20] P. Abratenko, *et al.* Search for an anomalous excess of charged-current quasielastic $\nu$e interactions with the MicroBooNE experiment using deep-learning-based reconstruction. *Physical Review D*, 105(11):112003, 2022.

[21] P. Abratenko, *et al.* Search for an anomalous excess of inclusive charged-current $\nu_e$ interactions in the MicroBooNE experiment using wire-cell reconstruction. *Physical Review D*, 105(11):112005, 2022.

[22] L. Bagby, *et al.* Overhaul and installation of the ICARUS-T600 liquid argon TPC electronics for the FNAL short baseline neutrino program. *JINST*, 16(01):P01037, 2021.

[23] M. Adamowski, *et al.* The liquid argon purity demonstrator. *JINST*, 9:P07005, 2014.

[24] C. Bromberg, *et al.* Design and operation of LongBo: A 2 m long drift liquid argon TPC. *JINST*, 10(07):P07015, 2015.

[25] Yichen Li, *et al.* A 20-liter test stand with gas purification for liquid argon research. *JINST*, 11(06):T06001, 2016.

[26] R. L. Workman, *et al.* Review of particle physics. *PTEP*, 2022:083C01, 2022.

[27] R. Acciarri, *et al.* Michel electron reconstruction using cosmic-ray data from the MicroBooNE LArTPC. *JINST*, 12(09):P09014, 2017.

[28] P. Abratenko, *et al.* Measurement of the flux-averaged inclusive charged-current electron neutrino and antineutrino cross section on argon using the NuMI beam and the MicroBooNE detector. *Physical Review D*, 104(5):052002, 2021.

[29] P. V. Vavilov. Ionization losses of high-energy heavy particles. *Soviet Physics JETP*, 5:749–751, 1957.

[30] M. Miyajima, T. Takahashi, S. Konno, T. Hamada, S. Kubota, H. Shibamura, and T. Doke. Average energy expended per ion pair in liquid argon. *Physical Review A*, 9:1438–1443, 1974.

[31] Z. Beever, D. Caratelli, A. Fava, F. Pietropaolo, F. Stocker, and J. Zettlemoyer. TRANSLATE — A Monte Carlo simulation of electron transport in liquid argon, November 2022.

[32] T. Doke, A. Hitachi, J. Kikuchi, K. Masuda, H. Okada, and E. Shibamura. Absolute scintillation yields in liquid argon and xenon for various particles. *Japanese Journal of Applied Physics*, 41(3A, Part 1):1538–1545, 2002.

[33] S. Amoruso, *et al.* Study of electron recombination in liquid argon with the ICARUS TPC. *Nuclear Instruments and Methods in Physics Research Section A: Accelerators, Spectrometers, Detectors and Associated Equipment*, 523:275–286, 2004.

[34] R. Acciarri, *et al.* A study of electron recombination using highly ionizing particles in the ArgoNeuT liquid argon TPC. *JINST*, 8:P08005, 2013.

[35] Measurement of the electronegative contaminants and drift electron lifetime in the MicroBooNE experiment. May 2016.

[36] Y. Li, C. Bromberg, M. Diwan, S. Kettell, S. Martynenko, X. Qian, V. Paolone, J. Stewart, C. Thorn, and C. Zhang. Parameterization of electron attachment rate constants for common impurities in LArTPC detectors May 2022.

[37] A. Lister and M. Stancari. Investigations on a fuzzy process: Effect of diffusion on calibration and particle identification in liquid argon time projection chambers. *JINST*, 17(07):P07016, 2022.

[38] G. Putnam and D. W. Schmitz. Diffusion changes the peak value of energy loss observed in a LArTPC, May 2022.

[39] P. Abratenko, *et al.* Measurement of the longitudinal diffusion of ionization electrons in the MicroBooNE detector. *JINST*, 16(09):P09025, 2021.

[40] Y. Li, *et al.* Measurement of longitudinal electron diffusion in liquid argon. *Nuclear Instruments and Methods in Physics Research Section A: Accelerators, Spectrometers, Detectors and Associated Equipment*, 816:160–170, 2016.

[41] M. Torti. Electron diffusion measurements in the ICARUS T600 detector. *Journal of Physics: Conference Series*, 888(1):012060, 2017.

[42] P. Abratenko, *et al.* Measurement of space charge effects in the MicroBooNE LArTPC using cosmic muons. *JINST*, 15(12):P12037, 2020.

[43] M. Antonello, *et al.* Study of space charge in the ICARUS T600 detector. *JINST*, 15(07):P07001, 2020.

[44] C. Adams, *et al.* A method to determine the electric field of liquid argon time projection chambers using a UV laser system and its application in MicroBooNE. *JINST*, 15(07):P07010, 2020.

[45] M. Babicz, S. Bordoni, A. Fava, U. Kose, M. Nessi, F. Pietropaolo, G.L. Raselli, F. Resnati, M. Rossella, P. Sala, F. Stocker, and A. Zani. A measurement of the group velocity of scintillation light in liquid argon. *Journal of Instrumentation*, 15(09):P09009–P09009, September 2020.

[46] D. A. Dwyer, *et al.* LArPix: Demonstration of low-power 3D pixelated charge readout for liquid argon time projection chambers. *JINST*, 13(10):P10007, 2018.

[47] D. Nygren and Y. Mei. Q-Pix: Pixel-scale signal capture for kiloton liquid argon TPC detectors: Time-to-charge waveform capture, local clocks, dynamic networks, September 2018.

[48] C. Adams, *et al.* Ionization electron signal processing in single phase LArTPCs. Part I. Algorithm description and quantitative evaluation with MicroBooNE simulation. *JINST*, 13(07):P07006, 2018.

[49] C. Adams, *et al.* Ionization electron signal processing in single phase LArTPCs. Part II. Data/simulation comparison and performance in MicroBooNE. *JINST*, 13(07):P07007, 2018.

[50] G. De Geronimo, *et al.* Front-end ASIC for a liquid argon TPC. *IEEE Transactions on Nuclear Science*, 58:1376–1385, 2011.

[51] Noise dependence on temperature and LAr fill level in the MicroBooNE time projection chamber, August 2015.

[52] M. Kuźniak and A. M. Szelc. Wavelength shifters for applications in liquid argon detectors. *Instruments*, 5(1):4, 2020.

[53] R. Acciarri, *et al.* Effects of nitrogen contamination in liquid argon. *JINST*, 5:P06003, 2010.

[54] A. A. Machado and E. Segreto. ARAPUCA a new device for liquid argon scintillation light detection. *JINST*, 11(02):C02004, 2016.

[55] A. A. Machado, E. Segreto, D. Warner, A. Fauth, B. Gelli, R. Maximo, A. Pizolatti, L. Paulucci, and F. Marinho. The X-ARAPUCA: An improvement of the ARAPUCA device, April 2018.

[56] L. Paulucci. The DUNE vertical drift photon detection system. *JINST*, 17(01):C01067, 2022.

[57] M. Auger, *et al.* A novel cosmic ray tagger system for liquid argon TPC neutrino detectors. *Instruments*, 1(1):2, 2017.

[58] C. Adams, *et al.* Design and construction of the MicroBooNE cosmic ray tagger system. *JINST*, 14(04):P04004, 2019.

[59] S. Amoruso, *et al.* Analysis of the liquid argon purity in the ICARUS T600 TPC. *Nuclear Instruments and Methods in Physics Research Section A: Accelerators, Spectrometers, Detectors and Associated Equipment*, 516:68–79, 2004.

[60] R. Acciarri, *et al.* Noise characterization and filtering in the MicroBooNE liquid argon TPC. *JINST*, 12(08):P08003, 2017.

[61] A. Abed Abud, *et al.* Reconstruction of interactions in the ProtoDUNE-SP detector with Pandora. June 2022.

[62] R. Acciarri, *et al.* The Pandora multi-algorithm approach to automated pattern recognition of cosmic-ray muon and neutrino events in the MicroBooNE detector. *European Physical Journal C*, 78(1):82, 2018.

[63] P. Abratenko, *et al.* Cosmic ray background rejection with wire-cell LArTPC event reconstruction in the MicroBooNE detector. *Physical Review Applied*, 15(6):064071, 2021.

[64] X. Qian, C. Zhang, B. Viren, and M. Diwan. Three-dimensional imaging for large LArTPCs. *JINST*, 13(05):P05032, 2018.

[65] A. Abed Abud, *et al.* Separation of track- and shower-like energy deposits in ProtoDUNE-SP using a convolutional neural network. *European Physical Journal C*, 82(10):903, 2022.

[66] R. Acciarri, *et al.* Convolutional neural networks applied to neutrino events in a liquid argon time projection chamber. *JINST*, 12(03):P03011, 2017.

[67] B. Abi, *et al.* Neutrino interaction classification with a convolutional neural network in the DUNE far detector. *Physical Review D*, 102(9):092003, 2020.

[68] P. Abratenko, *et al.* Convolutional neural network for multiple particle identification in the MicroBooNE liquid argon time projection chamber. *Physical Review D*, 103(9):092003, 2021.

[69] C. Adams, *et al.* Deep neural network for pixel-level electromagnetic particle identification in the MicroBooNE liquid argon time projection chamber. *Physical Review D*, 99(9):092001, 2019.

[70] P. Abratenko, *et al.* Semantic segmentation with a sparse convolutional neural network for event reconstruction in MicroBooNE. *Physical Review D*, 103(5):052012, 2021.

[71] R. Acciarri, *et al.* A deep-learning based raw waveform region-of-interest finder for the liquid argon time projection chamber. *JINST*, 17(01):P01018, 2022.

[72] P. Abratenko, *et al.* Neutrino event selection in the MicroBooNE liquid argon time projection chamber using Wire-Cell 3D imaging, clustering, and charge-light matching. *JINST*, 16(06):P06043, 2021.

[73] P. Abratenko, *et al.* Measurement of differential cross sections for $\nu_\mu$ - Ar charged-current interactions with protons and no pions in the final state with the MicroBooNE detector. *Physical Review D*, 102(11):112013, 2020.

[74] M. Antonello, *et al.* Muon momentum measurement in ICARUS-T600 LAr-TPC via multiple scattering in few-GeV range. *JINST*, 12(04):P04010, 2017.

[75] P. Abratenko, *et al.* Determination of muon momentum in the MicroBooNE LArTPC using an improved model of multiple Coulomb scattering. *JINST*, 12(10):P10010, 2017.

[76] S. Amoruso, *et al.* Measurement of the mu decay spectrum with the ICARUS liquid argon TPC. *European Physical Journal C*, 33:233–241, 2004.

[77] C. Adams, *et al.* Reconstruction and measurement of $\mathcal{O}(100)$ MeV energy electromagnetic activity from $\pi^0 \to \gamma\gamma$ decays in the MicroBooNE LArTPC. *JINST*, 15(02):P02007, 2020.

[78] R. Acciarri, *et al.* Michel electron reconstruction using cosmic-ray data from the MicroBooNE LArTPC. *JINST*, 12(09):P09014, 2017.

[79] P. Abratenko, *et al.* Electromagnetic shower reconstruction and energy validation with Michel electrons and $\pi^0$ samples for the deep-learning-based analyses in MicroBooNE. *JINST*, 16(12):T12017, 2021.

[80] R. Acciarri, *et al.* Convolutional neural networks applied to neutrino events in a liquid argon time projection chamber. *JINST*, 12(03):P03011, 2017.

[81] B. Abi, *et al.* Neutrino interaction classification with a convolutional neural network in the DUNE far detector. *Physical Review D*, 102(9):092003, 2020.

[82] P. Abratenko, *et al.* Semantic segmentation with a sparse convolutional neural network for event reconstruction in MicroBooNE. *Physical Review D*, 103(5):052012, 2021.

[83] C. Adams, *et al.* Deep neural network for pixel-level electromagnetic particle identification in the MicroBooNE liquid argon time projection chamber. *Physical Review D*, 99(9):092001, 2019.

[84] P. Abratenko, *et al.* Convolutional neural network for multiple particle identification in the MicroBooNE liquid argon time projection chamber. *Physical Review D*, 103(9):092003, 2021.

[85] A. Ereditato, I. Kreslo, M. Lüthi, C. Rudolf von Rohr, M. Schenk, T. Strauss, M. Weber, and M. Zeller. A steerable UV laser system for the calibration of liquid argon time projection chambers. *JINST*, 9(11):T11007, 2014.

[86] J. Conrad, B. J. P. Jones, Z. Moss, T. Strauss, and M. Toups. The photomultiplier tube calibration system of the MicroBooNE experiment. *JINST*, 10(06):T06001, 2015.

[87] W. Foreman, *et al.* Calorimetry for low-energy electrons using charge and light in liquid argon. *Physical Review D*, 101(1):012010, 2020.

[88] MicroBooNE Collaboration. Measuring light yield with isolated protons in MicroBooNE, August 2022. https://microboone.fnal.gov/wp-content/uploads/MICROBOONE-NOTE-1119-PUB.pdf.

[89] MicroBooNE Collaboration. Light yield calibration in MicroBooNE, August 2022. https://microboone.fnal.gov/wp-content/uploads/MICROBOONE-NOTE-1120-TECH.pdf.

[90] C. Adams, *et al.* Calibration of the charge and energy loss per unit length of the MicroBooNE liquid argon time projection chamber using muons and protons. *JINST*, 15(03):P03022, 2020.

[91] T. Yang. Calibration of calorimetric measurement in a liquid argon time projection chamber. *Instruments*, 5(1):2, 2020.